Liu, X., Jiang, J. Z., Titurus, B., & Harrison, A. (2018). Model identification methodology for fluid-based inerters. *Mechanical Systems and Signal Processing*, *106*, 479-494. https://doi.org/10.1016/j.ymssp.2018.01.018, https://doi.org/10.1016/j.ymssp.2018.01.018

Mechanical Systems and Signal Processing 106 (2018) 479–494

Contents lists available at ScienceDirect

Mechanical Systems and Signal Processing

journal homepage: www.elsevier.com/locate/ymssp

Model identification methodology for fluid-based inerters

Xiaofu Liu [a], Jason Zheng Jiang [a,*], Branislav Titurus [b], Andrew Harrison [a]

[a] Department of Mechanical Engineering, University of Bristol, Queens Building, University Walk, Bristol BS8 1TR, UK
[b] Department of Aerospace Engineering, University of Bristol, Queens Building, University Walk, Bristol BS8 1TR, UK

ARTICLE INFO

Article history:
Received 17 October 2017
Received in revised form 7 January 2018
Accepted 10 January 2018

Keywords:
Fluid
Inerter
Modelling
Identification
Damping
Helical-tube
Analogy
Hydraulic network

ABSTRACT

Inerter is the mechanical dual of the capacitor via the force-current analogy. It has the property that the force across the terminals is proportional to their relative acceleration. Compared with flywheel-based inerters, fluid-based forms have advantages of improved durability, inherent damping and simplicity of design. In order to improve the understanding of the physical behaviour of this fluid-based device, especially caused by the hydraulic resistance and inertial effects in the external tube, this work proposes a comprehensive model identification methodology. Firstly, a modelling procedure is established, which allows the topological arrangement of the mechanical networks to be obtained by mapping the damping, inertance and stiffness effects directly to their respective hydraulic counterparts. Secondly, an experimental sequence is followed, which separates the identification of friction, stiffness and various damping effects. Furthermore, an experimental set-up is introduced, where two pressure gauges are used to accurately measure the pressure drop across the external tube. The theoretical models with improved confidence are obtained using the proposed methodology for a helical-tube fluid inerter prototype. The sources of remaining discrepancies are further analysed.

1. Introduction

Using inerter-based vibration absorber for passive vibration control of mechanical systems has been a popular research topic since inerter's first introduction in 2002 [1]. Different from the mass element, it has the property that the force is proportional to the relative acceleration across the two terminals. The promising benefits of incorporating inerter into passive suspension system have been verified in various applications, which spread over a wide range of areas, including automotive engineering [2–4], civil engineering [5–7], railway engineering [8–11], and aerospace engineering [12].

The physical realisations of inerter may be classified into two main types, the flywheel-based and the fluid-based. For flywheel-based inerter, multiple experimental realisations were introduced with model parameters identified via experimental testing [13–16]. Effects of nonlinearities of these realisations, such as backlash and friction, were also investigated [17–19]. However, certain disadvantages are also exposed for flywheel-based inerters, such as excessive wear of transmission mechanism, which is the key factor restricts the real applications of inerter-based vibration absorbers. Meanwhile, there are two fluid-based inerter designs, the hydraulic inerter introduced in [20] and the helical-tube fluid inerter introduced in [21], both designs have the advantages of durability, structural simplicity and low cost, comparing to the flywheel-based design. This paper focuses on the study of a helical-tube fluid inerter design.

* Corresponding author.
E-mail address: z.jiang@bristol.ac.uk (J.Z. Jiang).

https://doi.org/10.1016/j.ymssp.2018.01.018
0888-3270/

It can be seen from previous work [21] that noticeable discrepancies between experimental results and available theoretical models exist, in particular for the damping effects. In [21], a model of the helical-tube fluid inerter was established, which contains various damping effects of the fluid. The model was also used to identify the device inertance and compliance. In [22], a nonlinear model of fluid inerter was taken into a full-car suspension model to investigate the potential improvement on reducing body accelerations by optimisation of suspension parameters. In the current paper, a lumped parameter hydraulic model, and an equivalent mechanical model have been established. By using these two models, the damping, inertance and stiffness effects in the mechanical network can be linked directly with the resistances, inertances and compliances in the hydraulic system. This analogy will not only help to understand the properties of fluid-based inerters better but also facilitates future design of hydraulic vibration absorption systems. Consequently, a system identification procedure for fluid-based inerter devices is followed. This procedure, by separating the identification of friction, stiffness and various damping effects, enables more accurate estimation of each parameter. Moreover, to measure the pressure drop across the external tube more precisely, two pressure gauges are fitted at the inlet and outlet. A nonlinear model that can accurately characterise the dynamic properties of a helical-tube fluid inerter prototype has been established.

This paper is organised as follows. Section 2 starts with an introduction to the working principle of fluid-based inerters, then a method to obtain the linear lumped parameter mechanical model equivalent to the hydraulic one, is proposed. A helical-tube fluid inerter prototype and the test rig are then introduced. In Section 3, a series of constant velocity tests are used to identify the friction and various damping effects. Identification of the stiffness effect is carried out in Section 4 to complete the full dynamic model. Comparison between the theoretical model and experimental data is then be presented, followed by analysis of the remaining discrepancies. Conclusions are drawn in Section 5.

2. Linear lumped parameter models and prototype design

This section first explains the working principle of fluid-based inerters. Analysis of the possible flow paths in the fluid-based inerter is then used to form the hydraulic network of the device. Following procedures, an equivalent mechanical network can be obtained. Subsequently, a helical-tube fluid inerter prototype is introduced, together with the test rig arrangement.

2.1. Working principle of fluid-based inerters

Fluid-based inerter uses the acceleration of the mass of fluid flowing through an external channel to produce axial inertance. The schematic plot of a helical-tube fluid inerter is shown in Fig. 1(a) as a typical design example. When the piston rod moves with velocity Δv relative to the cylinder under a force F towards the left, the working fluid flows through the external channel (as a helical tube in this example) with volume flow rate Q_1. The pressure inside each cylinder chamber is assumed to be homogeneously distributed, p_1 is the absolute pressure in the left chamber and p_2 is the absolute pressure in the right chamber. Typically, for these conditions, it can be assumed $p_1 > p_2$ when the rod is moving to the left. The pressure difference ($\Delta p = p_1 - p_2$) between two chambers is caused by the pressure drop across the inlet/outlet of the helical tube (Δp_{io}) and the pressure drop through the helical tube channel (Δp_h). Meanwhile, from the left to right, any hypothetical gap between the piston and the cylinder wall can provide an alternative route for the working fluid to flow with volume flow rate Q_2. This flow leads to a pressure drop Δp_s, where $\Delta p_s = \Delta p$. Apart from these physical flows, an induced flow with volume flow rate Q_3, which correspond to the compressibility effects of the fluid in the cylinder chamber might also exist. The fluid in the external channel is negligible due to its relatively small volume. Note that Q_3 is not included in Fig. 1(a) because it is a hypothetical flow path. Furthermore, the mechanical friction due to the seals is neglected for the derivations of the hydraulic network in Section 2.2. The mass of the piston is generally neglected due to its relatively low inertia.

2.2. Linear lumped parameter models

A fluid-based inerter produces effects such as damping, stiffness and inertance. Consider the flow paths described in Section 2.1, the main branch with flow rate Q_1 is through the external channel. This flow produces hydraulic inertance because of the mass of the fluid flowing through, and the hydraulic resistance due to the friction loss through the channel, as well as the flow restrictions at the inlet and outlet. Another considered flow branch represents the flow between the piston and the cylinder walls with flow rate Q_2. Furthermore, the compressibility effects of the fluid is modelled as an additional flow path between the terminals of the hydraulic system. The corresponding flow rate (Q_3) between the working volumes is [23]:

$$Q_3 = C\Delta\dot{p}, \tag{1}$$

where C is used to represent the effective hydraulic compliance [24].

In order to establish the linear lumped parameter models in both the hydraulic and mechanical domains, the relations between flow rates and pressure drops in the fluid-based inerter are assumed to be linear at this stage. The variables R_{io}, R_h and R_s are defined as the hydraulic resistances due to the inlet/outlet of the cylinder, the external channel and the leakage across the piston, respectively. The hydraulic inertance of the mass flowing through the external channel is defined as I [24]. These parameters are dependent on the fluid properties and prototype dimensions, which will be either specified or

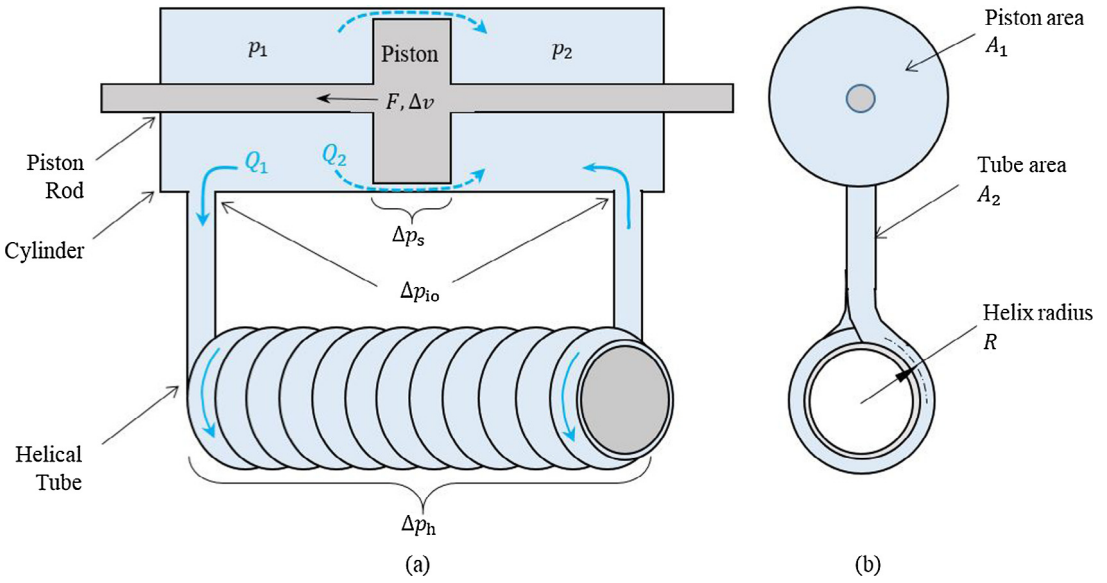

Fig. 1. The schematic of a helical-tube fluid inerter from (a) the side view and (b) the front view (the induced flow Q_3 is not denoted).

identified in the later sections. Based on the schematic shown in Fig. 1(a) and the considered flow branches, the hydraulic network of a typical fluid-based inerter can be constructed as shown in Fig. 2. The symbols used in the network are consistent with those defined in [25] for hydraulic resistance '⫪', hydraulic inertance '⩍' and hydraulic compliance '⎍'.

The total flow rate (Q) consists of individual flow rates through each branch:

$$Q = Q_1 + Q_2 + Q_3. \tag{2}$$

Similar to [24], the pressure difference between the cylinder's two chambers (Δp) can then be written as branch flow rates (Q_1 and Q_2) related:

$$\Delta p = R_h Q_1 + R_{io} Q_1 + I\dot{Q}_1 = R_s Q_2. \tag{3}$$

In the Laplace domain, substituting Eqs. (1) and (3) into Eq. (2), the relation between the total flow rate Q and pressure difference Δp can be derived: (s represents the complex variable and '∧' denotes the Laplace transform of the variables):

$$\hat{Q} = \left(R_s^{-1} + (R_h + R_{io} + Is)^{-1} + Cs\right)\Delta\hat{p}. \tag{4}$$

The terminal behaviour of an inerter device is usually characterised by the relation between the force through the device (F) and the relative terminal velocity (Δv) (defined in Section 2.1). These variables have following relations with the hydraulic ones,

$$F = A_1 \Delta p, \tag{5}$$

$$\Delta v = \frac{Q}{A_1}, \tag{6}$$

where A_1 is the effective piston area. Substituting Eqs. (5) and (6) into Eq. (4), the following equation is obtained,

$$\frac{\hat{F}}{\Delta\hat{v}} = \frac{{A_1}^2}{R_s^{-1} + (R_h + R_{io} + Is)^{-1} + Cs} = \frac{1}{\left(R_s A_1^2\right)^{-1} + \left(R_h A_1^2 + R_{io} A_1^2 + I A_1^2 s\right)^{-1} + C A_1^{-2} s}. \tag{7}$$

Notice that Eq. (7) now describes the terminal force-velocity behaviour of the device. If relevant network synthesis techniques are applied to Eq. (7) (e.g. [26,27]), the solution is not unique, which means multiple networks can be obtained. However, in order to link every mechanical component directly with the corresponding hydraulic component in Fig. 2, each hydraulic variable is transferred to its mechanical counterpart. In this way, the equivalent mechanical network is drawn, as shown in Fig. 3 with the corresponding admittance:

$$\frac{\hat{F}}{\Delta\hat{v}} = \frac{1}{c_s^{-1} + (c_h + c_{io} + bs)^{-1} + k^{-1}s}, \tag{8}$$

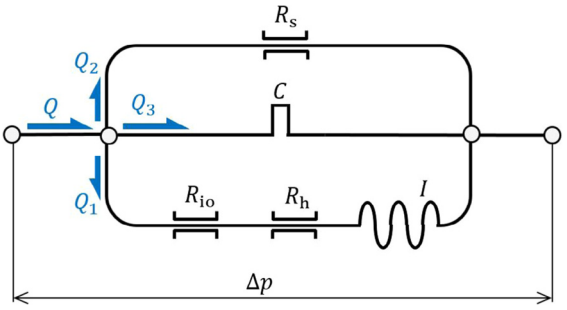

Fig. 2. The hydraulic network of a typical fluid-based inerter characterising the relation between the total flow rate Q and pressure difference Δp.

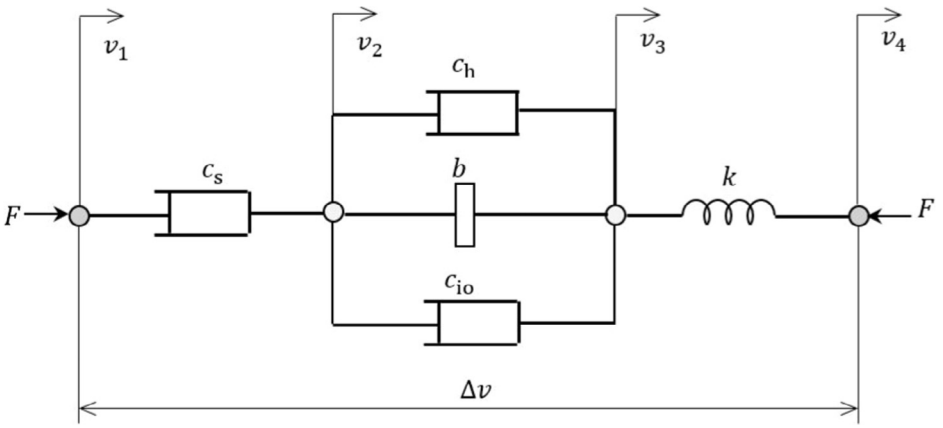

Fig. 3. The equivalent mechanical network of a typical fluid-based inerter characterising the relation between force F and relative terminal velocity Δv.

where the mechanical inertance $b = IA_1^2$, mechanical stiffness $k = A_1^2/C$, and mechanical damping c_{io}, c_h, c_s is equal to $R_{io}A_1^2, R_hA_1^2$ and $R_sA_1^2$, respectively. The symbol used for inerter '⫩' is consistent with [1], other symbols are the same as in [25]. It is worth to point that, following this procedure, the topology of the hydraulic network (Fig. 2) will always be the dual to the equivalent mechanical network (Fig. 3). This is because the mechanical through variable F [28] is proportional to the hydraulic cross variable Δp and similarly, the mechanical cross variable Δv is corresponding to the hydraulic through variable Q, see Eqs. (5) and (6).

Additionally, in Fig. 3, v_1 and v_4 are the velocities of each device terminals, where the relative terminal velocity $\Delta v = v_4 - v_1$; and v_2, v_3 represent internal velocities of the equivalent mechanical network. Variables $\Delta v_h, \Delta v_b$ and Δv_{io} are introduced to represent the relative terminal velocities of c_h, b and c_{io} in Fig. 3. Since these elements share the same terminals, $\Delta v_h = \Delta v_b = \Delta v_{io} = v_3 - v_2$. The advantage of the proposed procedure is that each flow rate through R_s, C, R_{io}, R_h and I in the hydraulic network relates to the relative velocity across c_s, k, c_{io}, c_h and b in the mechanical network, respectively, with the following equations,

$$v_3 - v_2 = \frac{Q_1}{A_1}, \tag{9}$$

$$v_2 - v_1 = \frac{Q_2}{A_1}, \tag{10}$$

$$v_4 - v_3 = \frac{Q_3}{A_1}. \tag{11}$$

Also, each relative pressure drop across R_s, C, R_{io}, R_h and I in the hydraulic network relates to the force through c_s, k, c_{io}, c_h and b in the mechanical network, in the similar way.

2.3. Prototype and test rig design

The prototype of a typical helical-tube fluid inerter was built at the University of Bristol for the purpose of testing, as shown in Fig. 4. It uses the independent helical tube coil, which is easy to replace the helical tubes with various diameters

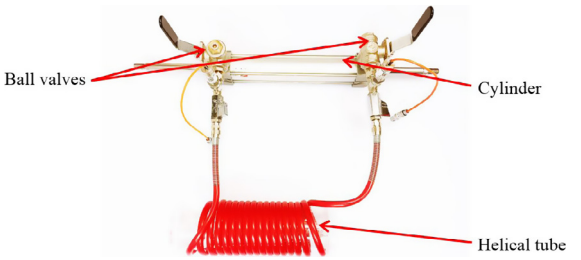

Fig. 4. The helical-tube fluid inerter prototype built at the University of Bristol.

and bend radiuses for comprehensive test requirements. The additional ball valves can partially isolate the cylinder chambers and helical tube channel, which enables fluid filling and helical tube replacement. Also, the two pressure gauges are designed to precisely record the working fluid pressures at the inlet and outlet of the helical tube. In this paper, all the theoretical and experimental results are based on this prototype, and its design parameters are listed in Table 1. Due to its low compressibility and cleanliness, water is used as the working fluid.

As shown in Fig. 5, the prototype of the helical-tube fluid inerter is placed on the customised test rig in the Automatic control and testing laboratory (ACTLab). The displacement-controlled excitations are generated by the hydraulic actuator (INSTRON PL25 kN), which is connected to the free end of the prototype. During the tests, the strut displacement across the prototype terminals is recorded by the LVDT (RDP DCTH6000C), which is placed in parallel with the inerter device. This configuration minimises the recorded backlash effects from the joints between the actuator and the prototype terminal. The strut force of the prototype is collected using the load cell(INSTRON 43629), which is located between the actuator and inerter piston rod. The two pressure gauges (Druck PDCR 822 15 bar) are placed at both ends of the helical tube to monitor the pressure changes in the helical tube during the tests.

Table 1
Parameters of the helical-tube fluid inerter prototype.

Description	Value
Piston area A_1[a] (m^2)	1.1×10^{-3}
Tube area A_2[a] (m^2)	2.8×10^{-5}
Helix radius R[a] (m)	0.0415
Helical tube length l (m)	5.59
Cylinder chamber length L (m)	0.217
Tube hydraulic diameter D_h (m)	0.006
Working fluid density ρ at 30 °C ($kg \cdot m^{-3}$)	995.6
Working fluid viscosity μ at 30 °C ($Pa \cdot s$)	7.98×10^{-4}

[a] Refer to Fig. 1(b).

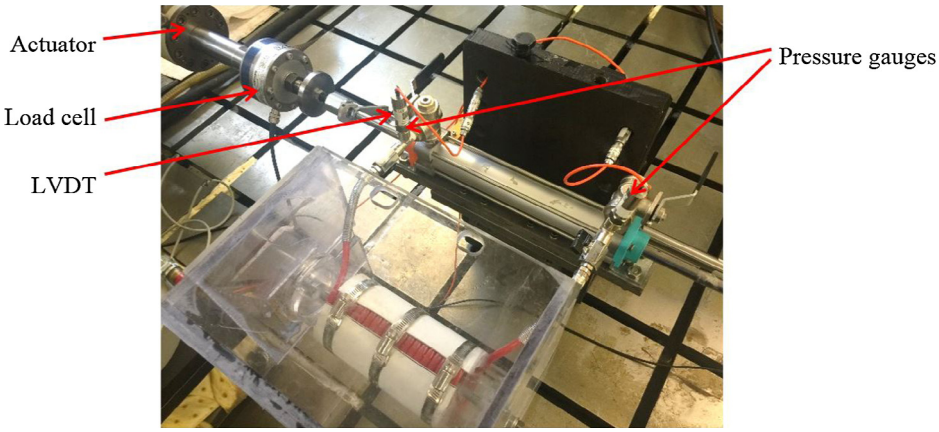

Fig. 5. The test rig for the helical-tube fluid inerter.

3. Friction and damping effects identification

In this section, the friction and damping effects of the fluid inerter prototype are experimentally tested and then identified. The constant velocity tests are carried out to produce the steady-state responses. Each test uses a triangular wave of displacement to excite the free end of the prototype, producing the constant strut velocities in both directions. Note that the transient phase of the velocity responses can also be used for parameter identification. It is decided to focus on the steady-state response with the purpose to separate the damping effects identification from the inertial and stiffness effects.

Assuming a constant velocity Δv_c and applying the final value theorem [29] to Eq. (8), the steady-state response can be described as:

$$\lim_{t\to\infty} F(t) = \lim_{s\to 0} s\hat{F}(s) = \lim_{s\to 0} s \times \frac{1}{c_s^{-1} + (c_h + c_{io} + bs)^{-1} + k^{-1}s} \times \frac{\Delta\hat{v}_c}{s} = \frac{1}{c_s^{-1} + (c_h + c_{io})^{-1}} \times \Delta\hat{v}_c. \tag{12}$$

Note that Eq. (12) shows that the stiffness and inertance terms will not affect the steady-state response. Using relevant network synthesis techniques, such as those introduced in [26], the network shown in Fig. 6 (excluding the friction term) can be obtained. Since the friction effects are mainly caused by the contact between the piston rod and cylinder seals, the additional friction term is considered in parallel with all other damping terms. The symbol '↗' included in Fig. 6 represents the possible nonlinearities in each corresponding damping term.

3.1. Friction and total damping force testing

The amplitude of 40 mm is chosen for the constant velocity tests, and the tests are carried out at strut velocities from 1.6×10^{-5} m/s to 0.224 m/s. The upper limit of the tested velocities is set by the maximum allowed force (4.5 kN) that can be applied to the strut terminal. During the tests, three sets of experimental data are collected. These include the strut displacements (x) by the LVDT, the strut forces (F) by the load cell, and the internal pressures at each end of the helical tube (p_1, p_2) by the pressure gauges.

To identify the steady-state strut force at each tested velocity, the method Least Absolute Residuals (LAR) [30] is used to fit a curve that minimises the sum of the absolute residuals, rather than the squares of the residuals. In this way, any extreme values in the transient response have less influence on the identified results. For example, in Fig. 7, the experimental strut force at strut velocity of 0.096 m/s has been fitted by a square wave with an amplitude of 0.296 kN, which is used as the

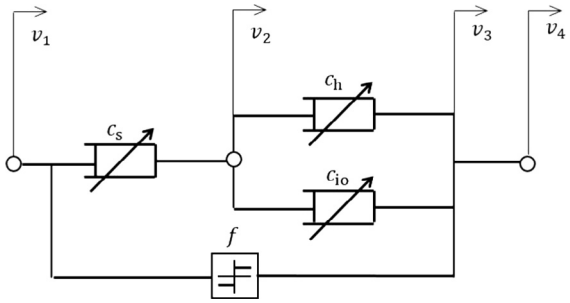

Fig. 6. The equivalent mechanical network of a typical helical-tube fluid inerter during the steady-state response, with a friction term included.

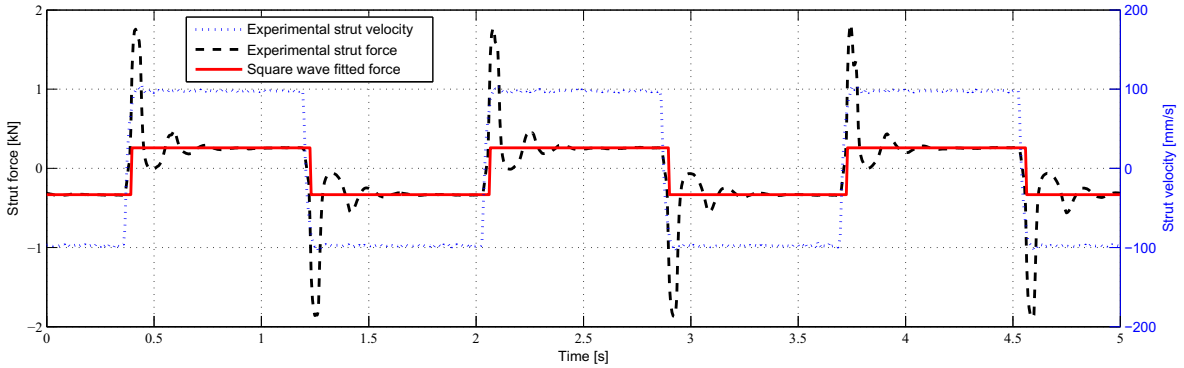

Fig. 7. Square wave fitting to a triangular wave test at the constant strut velocity of 0.096 m/s.

identified value of the steady-state strut force at this tested velocity. It is also worth mentioning that there is an initial load offset −0.0366 kN, which has been removed during post-processing of the load cell readings. At lower velocity, the friction dominates the response. Therefore, the steady-state strut force at the velocity equals 1.6×10^{-5} m/s is used to identify the friction force f, which equals approximately to 45 N. It is assumed that the friction of the tested prototype is constant in this study.

The difference between the two readings of the pressure gauges represents the pressure drop across the helical tube (Δp_h), which is equal to the sum of pressure drops caused by the hydraulic resistance (Δp_{hR}) and the hydraulic inertance (Δp_{hI}). One example is shown in Fig. 8, at the strut velocity of 0.096 m/s, where the steady-state pressure drop is identified to be approximately 210,000 Pa. For the steady-state response, it can be assumed that $\Delta p_{hR} = \Delta p_h = 210,000$ Pa since the pressure drop is purely caused by the hydraulic resistance. The initial values of the pressure gauges, which correspond to the atmospheric pressure, are set to 0 Pa. As a result, the pressure gauges during the experiments record both positive and negative values of the pressures.

The results of the damping tests at each tested strut velocity (Δv) are summarised in Fig. 9, with the red curve (solid line) representing the total hydraulic damping force (F_t) and the blue curve (dashed line) standing for the helical tube damping

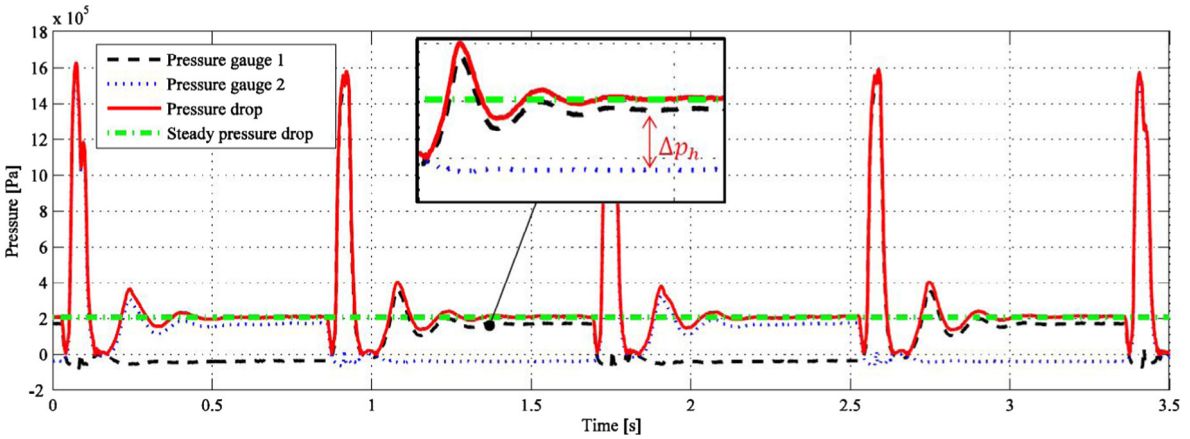

Fig. 8. The pressure drop across the helical tube at the strut velocity of 0.096 m/s.

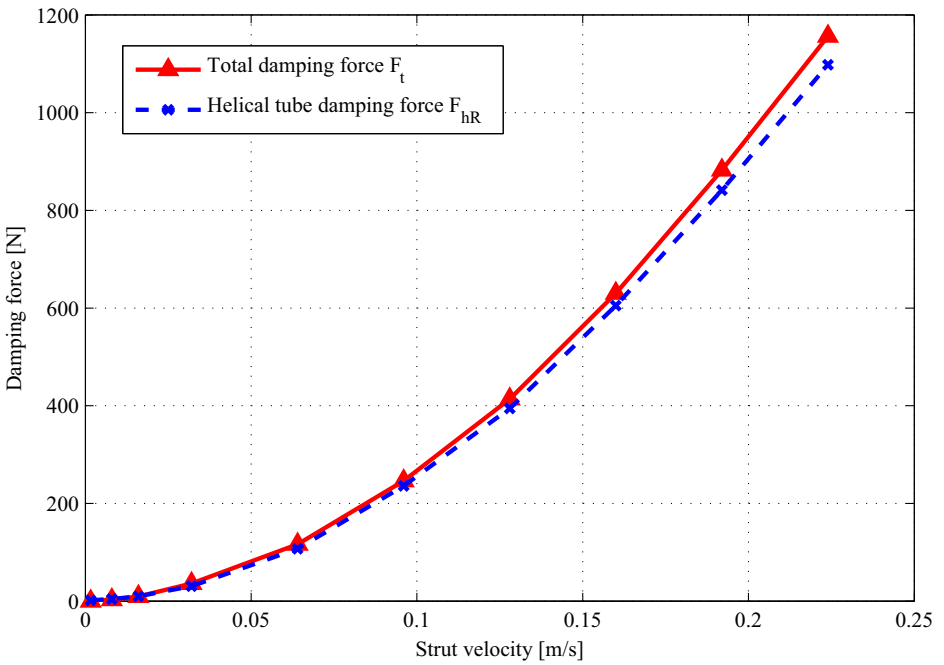

Fig. 9. Experimental total damping force and helical tube damping force versus strut velocity.

force due to the hydraulic resistance across the helical tube (F_{hR}). The total hydraulic damping force is calculated by subtracting the friction (f) from the strut force (F) recorded by the load cell. The helical tube damping force is calibrated from the formula $F_{hR} = A_1 \Delta p_{hR}$, where Δp_{hR} is the pressure drop across the pressure sensors. The differences between the red and blue curves in Fig. 9 are mainly caused by the extra damping from inlet/outlet between the cylinder and helical tube. It can be seen that the nonlinear damping properties are characterised by rapid damping force increase with the strut velocity. Furthermore, the total hydraulic damping force F_t is shown to be dominated by the helical tube damping as evidenced by the very small difference between these two lines. The observed discrepancy between these two values can be explained by the presence of potential leakage damping across the piston and tube inlet/outlet damping, both of which will be discussed in detail in the remaining part of this section.

3.2. Piston leakage damping identification

The damping caused by the potential flow leakage between the piston and the cylinder wall could influence the flow distribution inside the inerter. To accurately predict this damping effect, the hydraulic resistance due to the flow restriction of piston leakage (R_s) needs to be identified.

In order to test the leakage damping effect independently, both valves at the inlet/outlet of the cylinder are closed during the test. This action ensures that the flow between the two cylinder chambers can only pass through the leakage gap across the piston. The hydraulic network for this scenario can be constructed as shown in Fig. 10(a). Compared with Fig. 2, the flow paths with the flow rate of Q_2 passes through the potential leakage gap and Q_1 does not exist due to the blocked helical tube. In the meantime, Q_3 still exists, because of the presence of the compressibility effects of the fluid in the cylinder chamber. Following similar procedure discussed in Section 2.2, the equivalent mechanical network can be obtained, as shown in Fig. 10 (b).

Since the case of too small leakage gap will lead to extremely large leakage damping force (F_s), the lowest strut velocity of 1.6×10^{-5} m/s is applied to carry out the constant strut velocity test. The recorded strut force is shown as the black curve (solid line) in Fig. 11. Note that the strut force in the plot includes the extra friction term, which can be seen from the small strut force when the strut displacement equals zero. It can be observed that the strut force continuously increases until the safety load limit (4.5 kN) is triggered, which leads to the sudden switch off of the actuator and load cell before the strut displacement reaches 6 mm.

According to the steep increase of the strut force versus displacement curve in Fig. 11, it can be seen that the effective elastic force dominates the strut force. Consider the bulk modulus defined in [31],

$$B = V_1 \frac{\Delta p_1}{\Delta V} = V_2 \frac{-\Delta p_2}{-\Delta V}, \tag{13}$$

where B is the bulk modulus of fluid, ΔV is the change in volume, Δp_1 ($-\Delta p_2$) are the pressure changes in the left (right) cylinder chamber, and V_1 (V_2) are the volume of fluid in the left (right) cylinder chamber. The total volume of the cylinder chamber is denoted as V, which equals $V_1 + V_2$. Assuming the piston is placed in the centre position of the cylinder chamber, then $V_1 = V_2 = V/2$. Using Eq. (13) and $\Delta V = A_1 x$ (where x is the strut displacement), the effective elastic force due to the hydraulic compliance can then be expressed as:

$$F_k = A_1 \Delta p = A_1 (\Delta p_1 + \Delta p_2) = B \frac{4{A_1}^2}{V} x = kx, \tag{14}$$

Hence, the effective stiffness is shown to be proportional to the bulk modulus of fluid (B),

$$k = \frac{4{A_1}^2}{V} B. \tag{15}$$

The nominal bulk modulus of water is 2.2×10^9 N/m^2, and its value for air is 1.01×10^5 N/m^2. Compared with the experimental result, using Eq. (14), the corresponding effective elastic forces are plotted in Fig. 11 for the cylinder is full of water (blue dotted line), and when air occupies 1/100 of the cylinder chamber volume (red dashed line). The bulk modulus of the

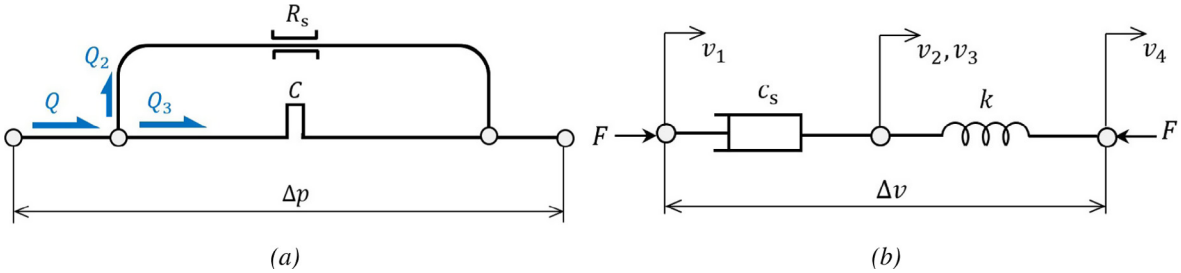

Fig. 10. A fluid-based inerter's (a) hydraulic network, and (b) equivalent mechanical network, with both valves at the inlet/outlet of the cylinder closed.

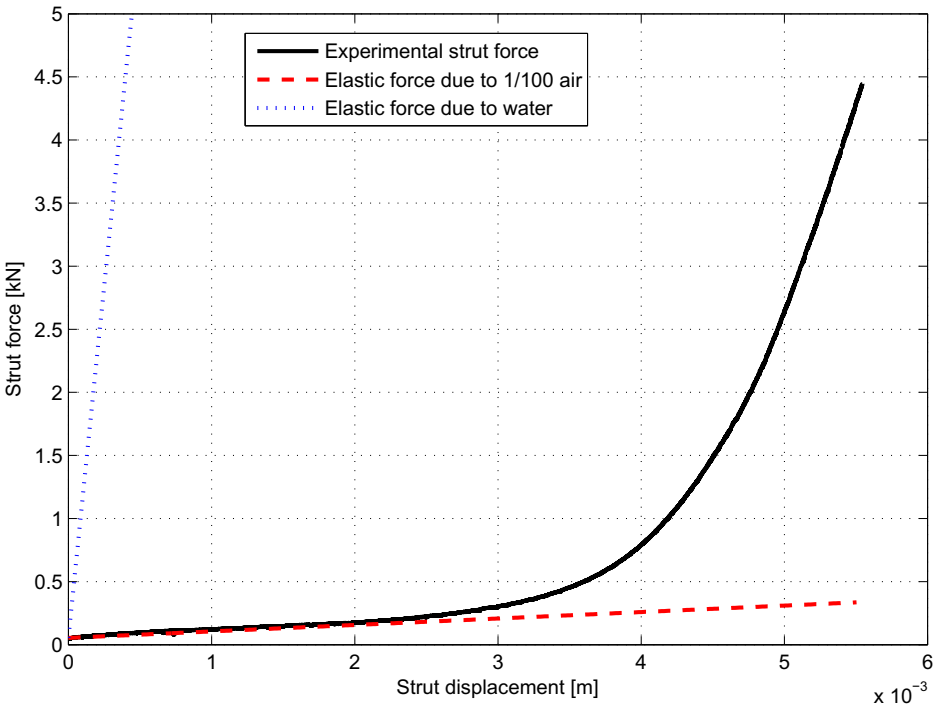

Fig. 11. The triangular wave test with constant velocity 1.6×10^{-5} m/s.

later case is calculated following the example from [31, p. 17]. The consistency between the experimental strut force and the elastic force for the 1/100 air occupation case during the initial 2 mm of the strut displacement gives the evidence of the presence of air inside the cylinder.

If the leakage damping force dominates the strut force, the initial transient response would be followed by a steady response. However, in Fig. 11, no such trend is observed, which means that the effect of leakage damping is very limited. Given the fact that all the tests in this paper are carried out within the same safety load limit, we assume there is no leakage damping, namely $R_s = c_s = \infty$, for the rest of this work.

3.3. Helical tube damping verification

From Fig. 9, it can be seen that the damping due to the hydraulic resistance inside the helical tube is the dominant damping effect. Its nonlinearities need to be investigated for an accurate theoretical modelling. Firstly, to determine whether the flow is laminar or turbulent, Reynold number (Re) of the flow in the helical tube is calculated using the formula:

$$Re = \frac{\rho D_h}{\mu} u = \frac{\rho D_h}{\mu} \frac{Q_1}{A_2}, \tag{16}$$

where u is the flow velocity in the tube (thus $Q_1 = A_2 u$) and other variables are defined in Table 1. According to the dimensions of the helical tube specified in Table 1, the curvature ratio λ of the helical tube is:

$$\lambda = \frac{D_h}{2R} = 0.072. \tag{17}$$

The critical Reynold number (Re_c), which represents the boundary between the laminar and turbulent flow for $\lambda < 0.1$ is given by [32]:

$$Re_c = 2100(1 + 12\lambda^{0.5}) = 8875. \tag{18}$$

After substituting $Re_c = 8875$ into Eq. (16), the boundary for laminar flow to become turbulent is at the flow rate of 4.19×10^{-5} m^3/s, which corresponds to strut velocity of 0.038 m/s. The tested flow rates in the helical tube are in the range from 1.7×10^{-6} m^3/s to 2.3×10^{-4} m^3/s with no leakage flow assumed. Therefore, most of the tested cases generate turbulent flow in the helical tube, the model based on the turbulent flow condition is required to fit the experimental results. Various analytical models based on experimental data were developed to estimate the pressure drop due to the hydraulic resistance across the helical-coiled tubes (Δp_{hR}). Most of these studies are based on the correlation between the Fanning fric-

tion factor (f_c) and Reynolds number, which is determined for specific fluid properties and tube characteristics. Using the notation introduced in Table 1, the equation for the pressure drop ($\Delta p'_{hR}$) due to hydraulic resistance of the flow in circular tube can be written as [33]:

$$\Delta p'_{hR} = f_c \frac{2\rho l}{D_h}\left(\frac{Q_1}{A_2}\right)^2. \tag{19}$$

The Fanning friction factor is calculated based on [34,35], where 6 different models are identified to be applicable to the tested flow with the certain Reynold number and curvature ratio. To select the most appropriate model for the tested helical tube in this study, the theoretical pressure drop across the helical tube ($\Delta p'_{hR}$) is calculated for each model using Eq. (19). The predicted pressure drops versus helical tube flow rate Q_1 (which equals to the total flow rate Q when no leakage is assumed) are plotted in Fig. 12(a). These pressures are compared with the experimental recorded Δp_{hR} (red dashed line). It can be observed that various discrepancies exist between the models and experiment. These discrepancies could originate from different test conditions such as dimension or material of the tubes used for the experiments. Among all of the formulas, the model introduced by White [36] matches the measured experimental results the best, which is denoted by the solid line in Fig. 12(a) with the corresponding values of the fitting error shown in Fig. 12(b).

Therefore, this model of the Fanning friction factor is used for theoretical modelling of the helical tube pressure drop due to hydraulic resistance. The model can be expressed as:

$$f_c = 0.08Re^{-1/4} + 0.012\sqrt{\frac{D_h}{2R}}. \tag{20}$$

Based on the assumed linear relation between the pressure drop and the flow rate through the helical tube: $\Delta p_{hR} = R_h Q_1$, the hydraulic resistance R_h is identified from Eq. (19), to be a Q_1-dependent coefficient,

$$R_h(Q_1) = f_c \frac{2\rho l}{D_h A_2^2} Q_1. \tag{21}$$

Apart from the main helical part of the tube, the pressure drop caused by the flow restrictions at the inlet and outlet of the tube (Δp_{io}) also needs to be considered for the modelling. One commonly used empirical formula for the inlet/outlet pressure drop [37] indicates:

$$\Delta p_{io} = \Delta p_{in} + \Delta p_{out} = 0.5\frac{\rho u^2}{2} + \frac{\rho u^2}{2} = 0.75\rho\left(\frac{Q_1}{A_2}\right)^2. \tag{22}$$

Therefore, based on the linear relationship between the pressure and flow assumed in Section 2.2, the hydraulic resistance due to the inlet/outlet of the tube is expressed as a Q_1-dependent coefficient:

$$R_{io}(Q_1) = \frac{\Delta p_{io}}{Q_1} = \frac{0.75\rho}{A_2^2} Q_1. \tag{23}$$

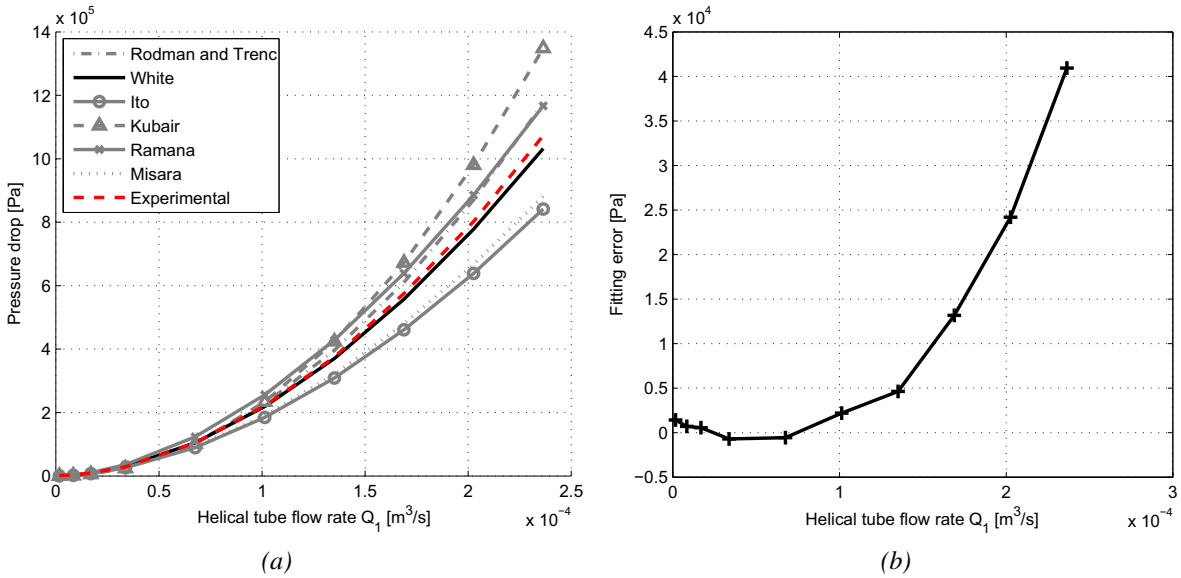

Fig. 12. (a) Comparison of the theoretical and experimental helical tube pressure drop versus flow rate, and (b) the fitting error between the chosen model (White) and the experimental data.

For the following construction of the model in the mechanical domain, the equivalent mechanical damping coefficients c_h and c_{io} are derived using Eqs. (21), (23), (9) and their respective relation with R_h and R_{io} defined in Section 2.2:

$$c_h = R_h A_1^2 = f_c \frac{2\rho l A_1}{D_h} \left(\frac{A_1}{A_2}\right)^2 \Delta v_h, \tag{24}$$

$$c_{io} = R_{io} A_1^2 = 0.75 \rho A_1 \left(\frac{A_1}{A_2}\right)^2 \Delta v_{io}. \tag{25}$$

These two equations will be used to represent the properties of damping in the theoretical model of the helical-tube fluid inerter prototype.

4. Dynamic model identification

In this section, two models for the helical-tube fluid inerter prototype are established. The inertance is calculated based on the physical properties of the device, and the effective stiffness is identified based on the comparison between the theoretical models and experimental testing results. Analysis of the remaining discrepancies is also provided.

4.1. Full theoretical models of the prototype

Based on the equivalent mechanical network in Fig. 3, the refined mechanical network of the prototype is shown in Fig. 13. This network includes the additional friction element due to the seals, the value of which has been identified to be 45 N in Section 3.1. The tube inlet/outlet damping (c_{io}) is represented as a velocity dependent term, using the nonlinear property described in Eq. (25). The leakage damping element (c_s) is treated as infinity based on the analysis in Section 3.2. The helical tube damping (c_h) can be represented by either theoretical formula or experimental data set. Thereby, two models are established using the network shown in Fig. 13:

- **Model 1** uses the theoretical formula Eq. (24) for c_h to calculate the damping force $F_{hR} = c_h \Delta v_h$. This type of model is able to reveal the influence of individual parameters of the damping force. It is also able to accommodate parameter values' changes within a certain range.
- **Model 2** uses a lookup table of the experimental data shown in Fig. 9 to find the value of F_{hR} (the strut velocity in Fig. 9 is equivalent to the relative velocity across the helical tube damping ($\Delta v_h = v_3 - v_2$) in Fig. 13 due to the fact that c_s from Fig. 3 can be treated as infinity). This model is expected to be more accurate because it includes properties that might not be captured by theoretical formulas, such as Eq. (24).

To complete the model, only the inertance and effective stiffness need to be identified. The inertance can be calculated theoretically using the principle of energy conservation with appropriate assumptions [21]. However, this work intends to investigate the connection between mechanical terminal behaviour (force and velocity) and the hydraulic variables. Therefore, the inertance is alternatively calculated based on Newton's second law. Under this law, the flow conditions in the tube can be characterised by the following equation:

$$m\dot{u} = F_{hI} \tag{26}$$

where $m = A_2 l \rho$ is the mass of fluid in the helical tube, and u is the flow velocity introduced in Section 3.3. Considering that Δp_{hI} is the pressure drop corresponding to hydraulic inertance, the hydraulic force $F_{hI} = \Delta p_{hI} A_2$. Then Eq. (26) can be written as:

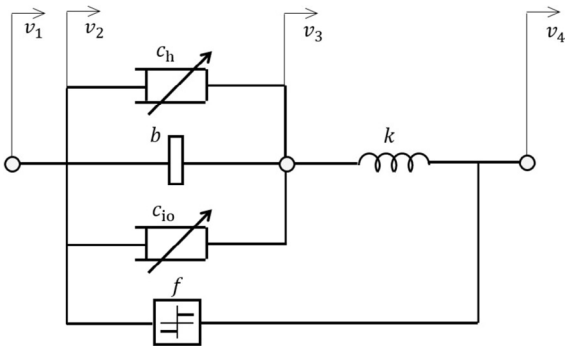

Fig. 13. The refined mechanical network of the helical-tube fluid inerter prototype.

$$(A_2 l\rho)\frac{\dot{Q}_1}{A_2} = \Delta p_{hl} A_2. \tag{27}$$

Noting that $\Delta p_{hl} = I\dot{Q}_1$ ([24]), it can be seen from Eq. (27), that $I = l\rho/A_2$, which is consistent with previous works [25,38]. Similar to [21], assuming the inertance of the fluid inside the cylinder chamber is negligible due to the relative small flow displacement and ignoring the influence of the temperature and unexpected air inside the tube, following the transformation from the hydraulic inertance to the mechanical inertance described in Section 2.2, the parameter b can be expressed as:

$$b = IA_1^2 = \frac{l\rho}{A_2}A_1^2. \tag{28}$$

This value can be calculated according to the prototype specifications in Table 1, the mechanical inertance is 219 kg. This value will be used for both Model 1 and Model 2.

In summary, the refined network in Fig. 13, Eqs. (24) and (20) are used to model the helical tube damping (c_h) [36], Eq. (25) is adopted to represent the tube inlet/outlet damping (c_{io}) [37], and the inertance is calculated by Eq. (28). The friction equals 45 N based on experimental testing introduced in Section 3.1. The stiffness k will be identified in Section 4.2.

4.2. Effective stiffness identification

With the calculated inertance value, the effective stiffness (k) is the only unknown parameter in the theoretical model. Similar to [21], its value is identified using the experimental data obtained from dynamic tests with sinusoidal excitations. Two Simulink models [39] are constructed corresponding to Model 1 and Model 2. To increase the accuracy of identification, the tests are carried out over a wide frequency range. However, the upper limits of the tested frequencies for each amplitude are restricted by the maximum allowed force that can be applied to the cylinder (4.5 kN). The test ranges are shown in Table 2. Amplitudes of 5 mm, 10 mm and 20 mm are chosen according to the potential strut strokes in most applications. The frequency range covers from 0.2 Hz up to 7 Hz. The experiment with the amplitude of 1 mm is more focused on higher frequency behaviour, for which the frequencies from 1 Hz to 13 Hz are tested. The frequency and amplitude range of experiment tests are of interest to the vibration suppression problem of many mechanical systems, such as road vehicles [3], multi-storey buildings [40], and railway vehicles [11].

With experimental data of strut displacement (x) and force (F), various nonparametric methods (e.g. those listed in [41]) can be adopted to identify the dynamic properties. The correlation method [42, p. 143] is chosen in this work to identify the transfer function from the relative terminal velocity Δv to the strut force F at each tested frequency. This method assumes the system to be linear at each frequency point. Based on the magnitude and phase of the network's dynamic responses across the tested frequency range, a metric J is introduced to quantify the percentage discrepancy between the experimental and theoretical results [43]:

$$J = \sum_{i=1}^{n_f} \frac{|Y(k, j\omega_i) - E(j\omega_i)|}{|E(j\omega_i)|}, \tag{29}$$

where n_f is the number of frequency points, $E(j\omega_i)$ is the experimental admittance function and $Y(k, j\omega_i)$ is the theoretically calculated admittance function based on either Model 1 or Model 2 (introduced in Section 4.1). The values of J for both models with each excitation amplitude are plotted in Fig. 14 as a function of the effective stiffness k.

The identified k values for Model 1 and Model 2 are determined based on the minimum values of J for each amplitude, which are listed in Table 3. The identified effective stiffness lies in the range of 0.24–1.31 MN/m. It can be seen that there is a significant difference between these values and the theoretical stiffness of the used fluid (approximate 40 MN/m for water at 30 °C). Similar observations are indicated in [21]. This discrepancy can be explained by the flexibility of the prototype joints and the presence of air in the cylinder [44,31]. The bulk modulus is highly sensitive to the pressure and the volume of the unexpected air in a certain volume of fluid [45], which could significantly reduce the effective stiffness k. One example in [31, p. 17] indicates that only 1% of the trapped air could cause 3 times less of the original bulk modulus of the fluid.

It is also noted from Fig. 14 and Table 3 that the values of the identified effective stiffness grow with the testing amplitude. This phenomenon can be explained as follows. From Eq. (15), it can be seen that k and B has a linear relation. It has been shown that higher pressures lead to bigger bulk modulus for liquid-gas mixture [31,46]. Based on Table 2, it can be seen that larger amplitude tests typically experience higher strut velocities, which corresponds to high pressures in the cylinder. Sim-

Table 2
Test range of amplitudes and frequencies.

Amplitude (mm)	1	5	10	20
Frequency (Hz)	1–13	0.2–7	0.2–4	0.2–2
Peak strut velocity (m/s)	0.004–0.052	0.004–0.14	0.008–0.16	0.016–0.16

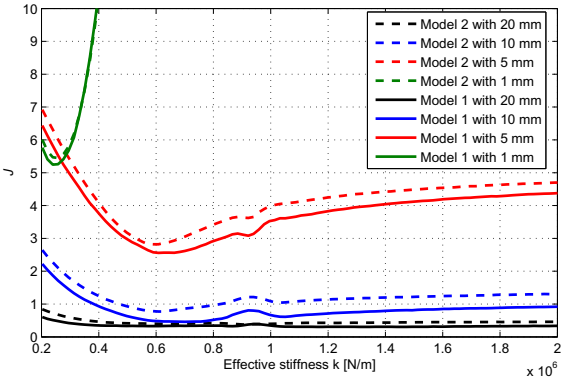

Fig. 14. The J value versus the effective stiffness k with amplitude 1 mm, 5 mm, 10 mm and 20 mm for Model 1 and Model 2.

Table 3
Identified values of effective stiffness for Model 1 and Model 2.

Amplitude (mm)		1	5	10	20
Identified effective stiffness (MN/m)	Model 1	0.24	0.64	0.70	1.31
	Model 2	0.25	0.60	0.62	0.92

ilar trend can be also observed from Fig. 11, where the gradient of the strut force versus displacement curve increases with the strut displacement.

In Table 3, the differences between identified k values for the same amplitude between Model 1 and Model 2 can be traced back to the fitting error of the chosen model (White [36]), as shown in Fig. 12(b). Furthermore, the J value corresponding to the identified k with amplitude 1 mm is much bigger than that with amplitude 5 mm, 10 mm and 20 mm, which could be caused by the inaccuracy of the friction model. The reason is that the smaller the testing amplitude is, the larger proportion of the total strut force the friction will occupy. Another possible reason is the presence of the unmodelled physics such as backlash in the prototype, which again will be more dominant with smaller amplitude tests.

4.3. Verification of the theoretical models

With the identified value of effective stiffness for each model and amplitude, the comparison between simulation results and the experimental data is displayed in Fig. 15. The transfer functions are shown as the Bode magnitude/phase plots of strut force over velocity. It can be seen that both models can accurately represent the properties of the tested prototype across the full range of frequencies. In Fig. 15(a)–(c), over the frequency range of 1–7 Hz, the gradient of approximately 20 dB/decade for the magnitude demonstrates the inertance dominated property. The evidence is also given by the peak values of the corresponding phase of approximately 20 to 30 degrees located between 2 Hz and 3 Hz. Although the phase of the ideal inerter should be 90 degrees, the reductions in phase could be caused by the presence of the damping and elastic effects. For frequencies below 1 Hz, the friction dominated performance leads to the increase in the magnitude of the transfer function with decreasing frequency. This is caused by the decrease in the strut velocity while the friction dominated force is approximately constant for given direction of piston motion. For higher frequency region (e.g. above 6 Hz for the 1 mm amplitude case), the compliance of the prototype dominates the performance, which gives rise to the decreasing magnitude. In addition, the worse quality of fitting between the experimental data and both theoretical models above 4 Hz in Fig. 15(d) is linked with the relatively inaccurate identification of the effective stiffness with the amplitude of 1 mm, shown in Fig. 14. Due to the restriction of the maximum allowed forces on the cylinder, there are no experimental data available for the stiffness dominated region in Figs. 15(a) and (b). As a result, it can also be observed from Fig. 14 that J is less sensitive to the effective stiffness change for larger amplitude, especially for the 10 mm and 20 mm cases. As a consequence, for larger amplitudes, the identification of the effective stiffness k based on the experimental data might be less representative.

With the values of inertance and effective stiffness determined, two theoretical models are established for the tested helical-tube fluid inerter. Both models are verified by comparing the simulation results to the experimental data, which show that the performance of tested prototype is well represented by the models across a wide frequency range. It can be seen from the results that qualitatively the frequency of 1–7 Hz is the inertance dominated range for a fluid-based inerter while the friction dominated behaviour appears below 1 Hz and the stiffness dominated behaviour is presented above 7 Hz. For the frequencies tested, the amplitudes between 5 and 20 mm are the most representative range for the fluid-based inerter while the less accurate model identification is found to be at the amplitude 1 mm. It can also be seen from Fig. 15 that good agreement between Model 1 and Model 2 are achieved in general, apart from the frequencies above 3 Hz for the 20 mm case. This can be explained by the larger fitting errors with higher flow rates, as shown in Fig. 12(b).

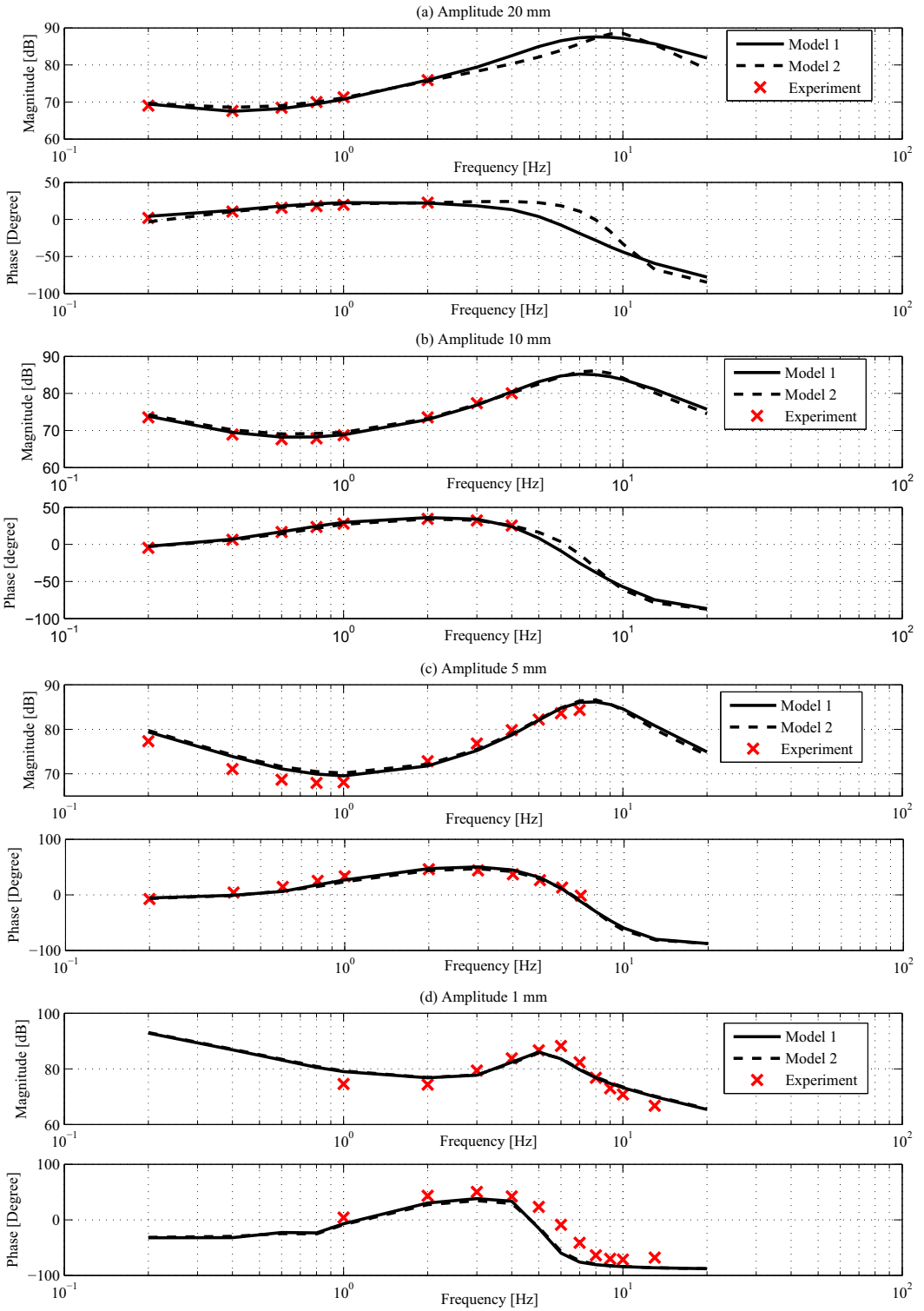

Fig. 15. Experimental data and model simulated results with identified values of effective stiffness from dynamic tests for amplitude (a) 20 mm, (b) 10 mm, (c) 5 mm, and (d) 1 mm.

In this work, the external tube of tested prototype is made of nylon to enable modular experimental setup. However, the metal tube can be used in practical applications for more robust performance. The identified model is still applicable for fluid inerter with metal tube since the properties are independent to the material of external tube.

5. Conclusions

This paper first presents a lumped parameter hydraulic model for fluid-based inerters, which allows the equivalent mechanical model to be established. In the process, the damping, inertance and stiffness elements in the mechanical model are mapped directly to the hydraulic resistance, inertance and compliance effects in the hydraulic model. Secondly, in order to enhance the modelling accuracy, a general model identification procedure is proposed, which enables different damping terms to be identified separately. Furthermore, an experimental set-up of pressure gauges are employed, which allows the helical tube damping to be more accurately identified. In the refined network of the helical-tube fluid inerter, the leakage damping is shown to be negligible, the theoretical formula for the helical tube damping is chosen by exploring the fitting error between multiple candidate models. Then the effective stiffness is identified based on the comparison between theoretical and experimental dynamic responses. Finally, the identified Model 1 and Model 2 of the tested prototype are verified by the good agreement between the simulation results of both models and the experimental data. In addition, the remaining discrepancies caused by unmodelled factors, such as the presence of air bubbles in the device, are also observed and analysed.

Funding

Jason Zheng Jiang is supported by an EPSRC grant [EP/P013456/1].

Acknowledgements

The authors would like to acknowledge Prof. Malcolm Smith for providing a University of Cambridge prototype fluid inerter for the authors' reference. The authors are thankful to Mr. Riccardo Ficca and Dr. Maciej Czechowicz of Jaguar Land Rover for their support through the development of this work.

Appendix A. Supplementary material

Supplementary data associated with this article can be found, in the online version, at https://doi.org/10.1016/j.ymssp.2018.01.018.

References

[1] M.C. Smith, Synthesis of mechanical networks: the inerter, IEEE Trans. Autom. Control 47 (2002) 1648–1662.
[2] S. Evangelou, D.J.N. Limebeer, R.S. Sharp, M.C. Smith, Mechanical steering compensation for high-performance motorcycles, J. Appl. Mech. 74 (2007) 332–346.
[3] M.C. Smith, F.C. Wang, Performance benefits in passive vehicle suspensions employing inerters, Veh. Syst. Dyn. 42 (2004) 235–257.
[4] F. Scheibe, M.C. Smith, Analytical solutions for optimal ride comfort and tyre grip for passive vehicle suspensions, Veh. Syst. Dyn. 47 (2009) 1229–1252.
[5] I.F. Lazar, S.A. Neild, D.J. Wagg, Using an inerter-based device for structural vibration suppression, Earthquake Eng. Struct. Dyn. 43 (2014) 1129–1147.
[6] I. Lazar, S. Neild, D. Wagg, Vibration suppression of cables using tuned inerter dampers, Eng. Struct. 122 (2016) 62–71.
[7] A. Giaralis, F. Petrini, Wind-induced vibration mitigation in tall buildings using the tuned mass-damper-inerter, J. Struct. Eng. 143 (2017) 04017127.
[8] J.Z. Jiang, A.Z. Matamoros-Sanchez, R.M. Goodall, M.C. Smith, Passive suspensions incorporating inerters for railway vehicles, Veh. Syst. Dyn.:Int. J. Veh. Mech. Mob. 50 (2012) 263–276.
[9] F.C. Wang, M.K. Liao, B.H. Liao, W.J. Su, H.A. Chan, The performance improvements of train suspension systems with mechanical networks employing inerters, Veh. Syst. Dyn. 47 (2009) 805–830.
[10] F.C. Wang, M.R. Hsieh, H.J. Chen, Stability and performance analysis of a full-train system with inerters, Veh. Syst. Dyn. 50 (2012) 545–571.
[11] J.Z. Jiang, A.Z. Matamoros-Sanchez, A. Zolotas, R. Goodall, M. Smith, Passive suspensions for ride quality improvement of two-axle railway vehicles, Proc. Inst. Mech. Eng., Part F: J. Rail Rapid Transit 229 (2015) 315–329.
[12] Y. Li, J. Jiang, S. Neild, Inerter-based configurations for main-landing-gear shimmy suppression, J. Aircraft (2016) 1–10.
[13] K. Ikago, K. Saito, N. Inoue, Seismic control of single-degree-of-freedom structure using tuned viscous mass damper, Earthquake Eng. Struct. Dyn. 41 (2012) 453–474.
[14] P. Brzeski, M. Lazarek, P. Perlikowski, Experimental study of the novel tuned mass damper with inerter which enables changes of inertance, J. Sound Vib. 404 (2017) 47–57.
[15] M. Lazarek, P. Brzeski, P. Perlikowski, Design and identification of parameters of tuned mass damper with inerter which enables changes of inertance, Mech. Mach. Theory 119 (2018) 161–173.
[16] C. Papageorgiou, N.E. Houghton, M.C. Smith, Experimental testing and analysis of inerter devices, J. Dyn. Syst. Meas. Control 131 (2008).
[17] F. Wang, W. Su, Inerter nonlinearities and the impact on suspension control, in: IEEE American Control Conference, 2008, pp. 3245–3250.
[18] A. Gonzalez-Buelga, I.F. Lazar, J.Z. Jiang, S.A. Neild, D.J. Inman, Assessing the effect of nonlinearities on the performance of a tuned inerter damper, Struct. Control Health Monitor. (2016).
[19] P. Brzeski, P. Perlikowski, Effects of play and inerter nonlinearities on the performance of tuned mass damper, Nonlinear Dyn. 88 (2017) 1027–1041.
[20] F.C. Wang, M.F. Hong, T.C. Lin, Designing and testing a hydraulic inerter, vol. 225, 2011, pp. 66–72.
[21] S.J. Swift, M.C. Smith, A.R. Glover, C. Papageorgiou, B. Gartner, N.E. Houghton, Design and modelling of a fluid inerter, Int. J. Control 86 (2013) 2035–2051.
[22] Y. Shen, L. Chen, Y. Liu, X. Zhang, Modeling and optimization of vehicle suspension employing a nonlinear fluid inerter, Shock Vib. (2016).
[23] B. Titurus, N. Lieven, Modeling and analysis of semi-active dampers in periodic working environments, AIAA J. 47 (2009) 2404–2416.
[24] R. Singh, G. Kim, P. Ravindra, Linear analysis of automotive hydro-mechanical mount with emphasis on decoupler characteristics, J. Sound Vib. 158 (1992) 219–243.
[25] J. Schonfeld, Analogy of hydraulic, mechanical, acoustic and electrical systems, Appl. Sci. Res. 3 (1954) 417–450.
[26] E.A. Guillemin, A summary of modern methods of network synthesis, Adv. Electron. Electron Phys. 3 (1951) 261–303.

[27] J.Z. Jiang, M.C. Smith, Regular positive-real functions and five-element network synthesis for electrical and mechanical networks, IEEE Trans. Autom. Control 56 (2011) 1275–1290.
[28] F. Firestone, A new analogy between mechanical and electrical systems, J.Acoust. Soc. Am. 4 (1933) 249–267.
[29] G.F. Franklin, J.D. Powell, A. Emami-Naeini, J.D. Powell, Feedback control of dynamic systems, vol. 3, Addison-Wesley, Reading, MA, 1994.
[30] A. Marazzi, Algorithms, Routines, and S Functions for Robust Statistics, Wadsworth & Brook/Cole, CA, 1993.
[31] H. Merritt, Hydraulic Control Systems, John Wiley & Sons, New York, 1967.
[32] S. Liu, A. Afacan, H. Nasr-El-Din, J. Masliyah, An experimental study of pressure drop in helical pipes, Proc. Roy. Soc. London A: Math. Phys. Eng. Sci. 444 (1994) 307–316.
[33] D. Rennels, H. Hudson, Pipe Flow: A Practical and Comprehensive Guide, John Wiley & Sons, 2012.
[34] S. Ali, Pressure drop correlations for flow through regular helical coil tubes, Fluid Dyn. Res. 28 (2001) 295–310.
[35] S. Rodman, F. Trenc, Pressure drop of laminar oil-flow in curved rectangular channels, Exp. Therm. Fluid Sci. 26 (2002) 25–32.
[36] C. White, Friction factor and its relation to heat transfer, Trans. Inst. Chem. Eng. 18 (1932) 66–68.
[37] B.S. Massey, J. Ward-Smith, Mechanics of fluids, vol. 1, CRC Press, 1998.
[38] A. Geisberger, Hydraulic engine mount modelling, parameter identification and experimental validation (Doctoral dissertation), University of Waterloo, 2000.
[39] MATLAB, SIMULINK, Ver. 8.1, Math Works, Natick, MA, 2008.
[40] S.Y. Zhang, J.Z. Jiang, S. Neild, Optimal configurations for a linear vibration suppression device in a multi-storey building, Struct. Control Health Monitor. 24 (2017).
[41] G. Kerschen, K. Worden, A. Vakakis, J.-C. Golinval, Past, present and future of nonlinear system identification in structural dynamics, Mech. Syst. Signal Process. 20 (2006) 505–592.
[42] L. Ljung, System Identification: Theory for the User, Prentice-Hall Inc., New Jersey, 1987.
[43] J.Z. Jiang, M.C. Smith, N.E. Houghton, Experimental testing and modelling of a mechanical steering compensator, in: The 3rd International Symposium on Communications, Control and Signal Processing (ISCCSP), 2008, pp. 249–254.
[44] B. Titurus, J.D. Bois, N. Lieven, R. Hansford, A method for the identification of hydraulic damper characteristics from steady velocity inputs, Mech. Syst. Signal Process. 24 (2010) 2868–2887.
[45] D. Ford, An analysis and application of a decoupled engine mount system for idle isolation, SAE Int. (1985).
[46] B. Titurus, Complete semi-analytical damper model identification using triangular displacement inputs, in: Proceedings of ISMA2014 including USD2014, 2014, pp. 3179–3188.